ACS Catalysis

Research Article

pubs.acs.org/acscatalysis

Pt/SBA-15 as a Highly Efficient Catalyst for Catalytic Toluene Oxidation

Yuan T. Lai,[†] Tse C. Chen,[‡] Yi K. Lan,[§] Bo S. Chen,[∥] Jiann H. You,[∥] Chia M. Yang,[⊥] Nien C. Lai,[⊥] Jia H. Wu,[†] and Ching S. Chen*[,†]

[†]Center for General Education, Chang Gung University, 259 Wen-Hwa first Road, Kwei-Shan Tao-Yuan, Taiwan 333, Republic of China

[‡]Department of Pathology, Chang Gung Memorial Hospital, 5 Fusing Street, Kwei-Shan Tao-Yuan, Taiwan 333, Republic of China

[§]Department of Chemical Engineering, National Tsing Hua University, Kuang-Fu Road, Hsinchu, Taiwan 300, Republic of China

[∥]Department of Chemical and Materials Engineering, Chang Gung University, 259 Wen-Hwa first Road, Kwei-Shan Tao-Yuan, Taiwan 333, Republic of China

[⊥]Department of Chemistry, National Tsing Hua University, Hsinchu, Taiwan 300, Republic of China

Supporting Information

ABSTRACT: The catalytic oxidation of toluene has been investigated using a series of Pt/SBA-15 and Pt/SiO_2 catalysts, and the Pt/SBA-15 catalyst exhibits significantly higher catalytic activity for the oxidation of toluene than the Pt/SiO_2 catalysts. The SBA-15-supported Pt nanoparticles possess the ability to strongly dissociate toluene to benzene, hydrocarbon fragments (CH_x), and H_2 at low temperatures, but the Pt/SiO_2 catalysts are nonreactive toward the decomposition of toluene. The products resulting from the dissociation of toluene were easily oxidized by oxygen, thereby positively affecting the conversion rate of toluene oxidation on Pt/SBA-15. Temperature-programmed desorption measurements clearly indicate that the dissociation reaction mainly consists of breakage of the C−C bonds between the phenyl and methyl groups. Combined density functional theory (DFT) calculations and DRIFT spectroscopy are carried out to investigate the stretching frequency of CO adsorbed on the defect sites of various Pt clusters, suggesting that the subnanosized Pt particles (icosahedron cluster) and/or Pt single atom may be formed in the structure of SBA-15. Pt sites associated with low coordination and subnanoscale Pt particles and/or single Pt atoms in the SBA-15 support can facilitate toluene adsorption and induce strong dissociation.

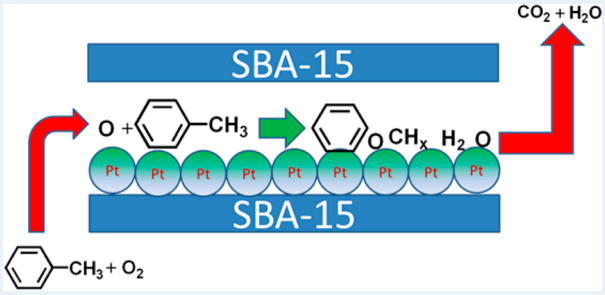

KEYWORDS: *toluene oxidation, Pt/SBA-15, IR spectroscopy, temperature-programmed desorption, density functional theory*

1. INTRODUCTION

Volatile organic compounds (VOCs) are carbon-based chemicals that can cause environmental and health problems. Therefore, the development of effective and reliable methods for the complete elimination of VOCs is important because of their harmful effects on human health and their contribution to air pollution in the environment. VOCs that are suspected to be endocrine-disrupting chemicals, such as benzene, toluene, and xylene, are of particular concern due to their high toxicity to humans. These aromatic derivatives are frequently used in making paints, adhesives, rubbers, and in leather tanning processes because of their excellent ability to dissolve organic substances. The catalytic oxidation of VOCs has been recognized as an economical process for VOC elimination, even at low concentrations (250−1000 ppm).[1−3] Supported platinum catalysts are widely used for the catalytic oxidation of VOCs in the environmental control of effluent gases.[4] Kinetic studies, the particle sizes of Pt-based catalysts, and the effects of several promoters on toluene oxidation have been widely discussed in the literature.[5−15]

To date, enhancing the efficiency of these Pt catalysts is still an important goal due to the high cost of Pt metal. In general, support materials with high surface areas play an important role in the efficiency of noble metals through numerous parameters, including support−metal interactions and better metal dispersion. Recently, mesoporous SBA-15 silica has been identified as a promising support for metal particles because of its high surface area (600−1000 m^2/g).[16−23] SBA-15 possesses a hexagonal arrangement of uniform channels and pore diameters that range from 5 to 30 nm. During the preparation of Pt nanoparticles, SBA-15 mesoporous materials are frequently used to improve Pt dispersion and to obtain nanosized and/or tiny Pt particles because the SBA-15

Received: May 29, 2014
Revised: September 17, 2014
Published: September 18, 2014

   dx.doi.org/10.1021/cs500733j | ACS Catal. 2014, 4, 3824−3836

materials have a high surface area and an ordered structure.[24] Bendahou et al. have reported that Pt/SBA-15 and Pd/SBA-15 catalysts can give high activity for the deep oxidation of toluene, and the addition of lanthanum may lead to lower reaction efficiency on these Pt and Pd catalysts.[25] However, the reason for high reactivity for toluene oxidation on Pt/SBA-15 and Pd/SBA-15 catalysts has still attracted little attention. On the other hand, the dependence of active sites and decomposition on toluene adsorption versus the efficiency of the catalytic oxidation reaction on very small Pt particles has attracted minimal discussion in the literature. Herein, we report a simple wet impregnation method for obtaining Pt nanoparticles on SBA-15. The catalytic activity for the oxidation of toluene is examined on Pt/SBA-15 and Pt/SiO_2 catalysts. A series of temperature-programmed desorption (TPD) and IR experiments are used to compare the dissociation and oxidation behaviors of toluene on Pt/SBA-15 and Pt/SiO_2.

2. EXPERIMENTAL SECTION

2.1. Catalyst Preparation. Mesoporous SBA-15 silica was synthesized by adding 40.2 g tetraethoxysilane (TEOS) to a premixed solution of 10.8 g of 35% HCl solution and 18.7 g Pluronic P-123 ($EO_{20}PO_{70}EO_{20}$), which yielded a mixture with a molar composition of 1 TEOS/0.017 P-123/0.54 HCl/100 H_2O. The mixture was stirred at 308 K for 24 h and further aged at 363 K for 24 h. The product was filtered and dried at 363 K. The as-synthesized SBA-15 was calcined at 813 K for 6 h to remove the copolymer template. The Pt/SBA-15 and Pt/SiO_2 catalysts were prepared by impregnating 1 g of SBA-15 or SiO_2 (Sigma-Aldrich, 300 m^2/g) samples with 20 mL of 5.1×10^{-4} M and 2.3×10^{-3} M aqueous H_2PtCl_6 to prepare 0.2% and 0.9% Pt catalysts.

All of the Pt catalysts were calcined in air and reduced under H_2 at 673 K for 5 h before use.

2.2. Measurement of the FT-IR Spectra. The in situ DRIFT analysis of CO and toluene adsorption was performed using a Nicolet 5700 FTIR spectrometer equipped with a mercury cadmium telluride (MCT) detector; the instrument was operated at a 1 cm^{-1} resolution for 256 scans. The DRIFT cell (Harrick) was equipped with ZnSe windows and with a heating cartridge that allowed the sample to be heated to 773 K. IR spectra of the CO adsorption on Pt/SBA-15 were obtained using pure CO that was passed through Pt/SBA-15 samples for 30 min at room temperature; the residual gaseous CO was purged using a He stream for 60 min. Toluene was dosed onto all catalysts by injection with a 10 μL Hamilton 7001 syringe through a port located upstream of the DRIFT cell. The injection port, which was similar to that used in gas chromatography, was heated to 373 K to prevent the condensation of toluene.

2.3. Measurement of the Platinum Surface Area. The Pt contents in the Pt/SBA-15 and Pt/SiO_2 samples were measured by inductively coupled plasma mass spectrometry (ICP/MS), which was performed at the High Valued Instrument Center of the National Sun Yat-sen University, Taiwan. The Pt surface areas of the Pt/SBA-15, and Pt/SiO_2 catalysts were measured via saturated CO chemisorption at room temperature in a glass vacuum system. All Pt catalysts were calcined in air and reduced under H_2 at 673 K for 5 h before CO chemisorption. The Pt sample disk was made of 0.2 g catalyst pressed at 260 atm, which was repeatedly reduced in 760 Torr H_2 at 673 K for 2 h and evacuated at 673 K at 4×10^{-5} Torr in the glass vacuum system for 30 min. Twenty Torr of CO was introduced to the catalyst at room temperature for 10 min to obtain uptake saturation. The surface area of Pt catalyst was calculated assuming CO/Pt stoichiometric ratio of 1. The average surface density of the Pt metal was 7.1×10^{18} Pt atoms/m^2.[26]

2.4. Brunauer–Emmett–Teller (BET) Measurements. N_2 physisorption isotherms were measured at 77 K using a Quantachrome Autosorb-1-MP instrument. Brunauer–Emmett–Teller (BET) surface areas were calculated from the adsorption branches in the relative pressure range of 0.05–0.30. The isotherms were analyzed by the nonlocal density functional theory (NLDFT) method to evaluate pore sizes of the samples using the kernel of NLDFT equilibrium capillary condensation isotherms of nitrogen at 77 K on silica (adsorption branch, assuming cylindrical pore geometry) and total pore volumes were evaluated at a relative pressure of 0.95.

2.5. Small- and Wide-Angle X-ray Diffraction (XRD) Measurements. The structures of the SBA-15 before and after Pt deposition were identified by a small-angle XRD spectra recorded on a MacScience MXP18AHF spectrometer with a Cu Kα radiation source (0.1549 nm). The wide angle of XRD spectra of Pt/SBA-15 and Pt/SiO_2 for Pt diffraction patterns scanning from 20 to 70° (2θ) were performed using Rigaku Miniflex II equipped with a Cu Kα radiation (0.1549 nm).

2.6. Catalytic Tests for Toluene Oxidation. All toluene oxidation reactions were performed in a fixed-bed reactor (0.95 cm inner diameter) at atmospheric pressure. A thermocouple connected to a PID temperature controller was placed on top of the catalyst bed. The toluene oxidation reactions were performed using an air stream with a total flow rate of 30 mL/min passing through liquid toluene at 273 K, and the resulting mixture of O_2/toluene with a 22.5/1 molar ratio was passed over 20 mg of catalyst. The conversion of the reaction was maintained at less than 10% to ensure that the conditions were similar to differential conditions. All products were analyzed via gas chromatography (GC) through a 12-ft Porapak-Q column; the gas chromatograph was equipped with a thermal conductivity detector (TCD). The turnover frequency (TOF) was calculated using the following formula: TOF = [conversion $\times$0.003 (mL/s for toluene) $\times$ 6.02×10^{23} (molecules/mol)]/[24400 (mL/mol) $\times$ Pt sites]. Carbon balance data were measured from the peak areas corresponding to toluene and CO_2 in the chromatograms throughout the experiment over the temperature range, which were good at around 95–100%.

2.7. Temperature-Programmed Desorption (TPD). TPD experiments were performed in a 100 mL/min stream of He at atmospheric pressure in a conventional flow system. The temperature was increased from 300 to 773 K at a rate of 10 K/min over the course of the TPD process. All of the signals were measured with a VG Smart IQ+ 300D mass spectrometer. The temperature was measured with a K-type thermocouple, which was inserted into the catalyst bed, and the desorbed products were introduced into the vacuum chamber through a leak valve using He as the carrier gas. The operating pressure in the chamber was approximately 3×10^{-7} Torr, and the base pressure in the chamber was approximately 2×10^{-9} Torr. The catalysts were dosed with toluene via injection using a 10 μL Hamilton 7001 syringe, which was inserted through a port located upstream of the quartz reactor. The injection port, which was similar to that used in gas chromatography, was heated to 373 K to prevent the condensation of toluene.

2.8. Density Functional Theory (DFT) Calculations. The DFT-based methods were performed to calculate the

dx.doi.org/10.1021/cs500733j | ACS Catal. 2014, 4, 3824–3836

vibrational frequency of CO adsorption on Pt surfaces. All DFT calculations were performed using *Accelrys Materials Studio* equipped with DFT package DMol3. The wave functions are expanded in terms of numerical basis sets in DMol3.[27] Considering no hydrogen in our system, DND, the double-numeric quality basis set with d-functions was chosen. The gradient-corrected GGA functional and the specific functional PW91 developed by Perdew and Wang were selected for the exchange−correlation potential in the DFT calculations.[28] To improve the computational performance and speed up the SCF convergence, the Fermi smearing of 0.005−0.01 hartree, a real-space cutoff of 4 Å and the direct inversion in an iterative subspace (DIIS, size = 6−9) were used. For the geometry optimization, the tolerances of energy, gradient, and displacement convergence were set as 2.0×10^{-5} hartree, 0.004 hartree/Å, and 0.005 Å, respectively. Within this DFT setting, the stretching frequency of single CO molecule was calculated as 2121 cm^{-1}, which has ∼2.0% error compare to the experimental value 2170 cm^{-1}.

3. RESULTS

3.1. Characterization of the Pt/SBA-15 and Pt/SiO_2 Catalysts. Figure 1 shows the small-angle XRD patterns of the

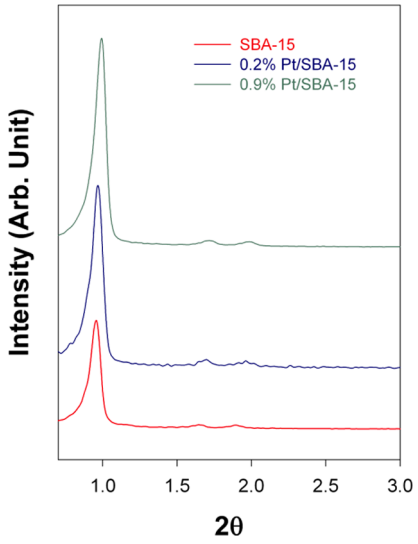

Figure 1. Small-angle XRD patterns for the SBA-15 and Pt/SBA-15 samples.

SBA-15 support with and without the reduced Pt nanoparticles. Each spectrum exhibited three well-resolved diffraction peaks in the region of $2\theta = 0.5-2.0°$, which were indexed to the (100), (110), and (200) planes that are characteristic of a material with 2D hexagonal symmetry. The formation of reduced Pt particles may cause a slight shift in the diffraction peaks toward higher angles relative to the peaks of the SBA-15 support due to a contraction of the framework accompanied by a decrease in the cell parameter a_0.

The textural properies of the mesoporous materials both with and without Pt particles were examined using N_2 physisorption measurements (Figure 2A). The textural properties that were obtained from the N_2 physisorption measurements are summarized in Table 1. All of the samples exhibited type IV adsorption isotherms. A hysteresis loop with a sloping adsorption branch and a relatively sharp, steep desorption branch was observed at the relative pressure (P/P_0). The presence of H1-type hysteresis loop suggests that the mesoporous channels remained cylindrical after the deposition of Pt particles. The pore size distributions of the samples, which were calculated from the N_2 adsorption isotherms using the kernel of the nonlocal density functional theory (NLDFT) equilibrium capillary condensation isotherms of nitrogen at 77 K on silica (adsorption branch, assuming cylindrical pore geometry), are presented in Figure 2B. The average pore size of the SBA-15 with the Pt particles was slightly smaller than that of the SBA-15 and was centered at 6.8 nm. This is contributed from the contraction of silica walls during the heat treatment, which is consistent with the observation of the peak shift in the XRD patterns. The deposition of Pt nanoparticles in the SBA-15 support also decreased the accessible pore volume and surface area as the Pt concentration increased.

The Pt surface areas and amounts of CO adsorbed are summarized in Table 2. The Pt surface areas of the Pt/SBA-15 and Pt/SiO_2 catalysts used in the experiments were measured via saturated CO chemisorption at room temperature. Figure S1 shows the X-ray diffraction (XRD) patterns of the face-centered cubic (fcc) Pt structures on the SiO_2 and SBA-15, which exhibited peaks at $2\theta = 39.6°$ and 46.0°; these peaks correspond to the (111) and (200) facets, respectively.The average particle size of all the reduced Pt/SBA-15 and Pt/SiO_2 samples was calculated from the Pt(111) peak according to the Scherrer equation using the full width at half-maximum (fwhm) values. The XRD signals of 0.2 wt % Pt/SBA-15 were too weak to discriminate from background. It was found that Pt deposited on SBA-15 can offer higher Pt surface area and smaller Pt particle size.

The HRTEM images for all Pt/SBA-15 catalysts are shown in Figure 3. It is evident that the Pt particles could apparently form inside of the channels of SBA-15 (images a and b). For the 0.2% Pt/SBA-15, the tiny Pt particles less than 1 nm dispersed in the SBA-15 structure could be observed. This finding suggested a reasonable interpretation why no detectable XRD patterns (Figure S1) could be found for 0.2% Pt/SBA-15. As Pt loading increased to 0.9% deposited on SBA-15, the size of Pt particles on SBA-15 was not very uniform. Several Pt particles completely filled the channels, but there were still many smaller particles that could disperse in the SBA-15 structure.

3.2. Catalytic Toluene Oxidation over Pt/SBA-15 and Pt/SiO_2 Catalysts. The dependences of the specific turnover frequency as a function of temperature for the Pt/SiO_2 and Pt/SBA-15 catalysts are shown in Figure 4A. The only products detected during the oxidation reaction were carbon dioxide and water. The toluene oxidation turnover rate on the Pt/SiO_2 and Pt/SBA-15 catalysts increased as the Pt loading decreased. However, the 0.2 and 0.9 wt % Pt catalysts supported on SBA-15 showed higher catalytic activity than all other Pt/SiO_2 catalysts. The Arrhenius plots that provide the apparent activation energies for toluene oxidation on all of the Pt/SiO_2 and Pt/SBA-15 catalysts are shown in Figure 4B. The apparent activation energies for toluene oxidation between 373 and 473 K on these Pt catalysts increased in the following order: 0.2 wt % Pt/SBA-15 < 0.9 wt % Pt/SBA-15 < 0.2 wt % Pt/SiO_2 < 0.9 wt % Pt/SiO_2.

3.3. Temperature-Programmed Desorption (TPD). Figure 5 presents the TPD spectra of toluene (1−10 μL) on 0.9 wt % Pt/SBA-15; toluene (92 amu), benzene (78 amu), and H_2 (2 amu) were monitored by QMS during the course of the TPD process. When low doses (1 μL) were used, the toluene,

dx.doi.org/10.1021/cs500733j | *ACS Catal.* 2014, 4, 3824−3836

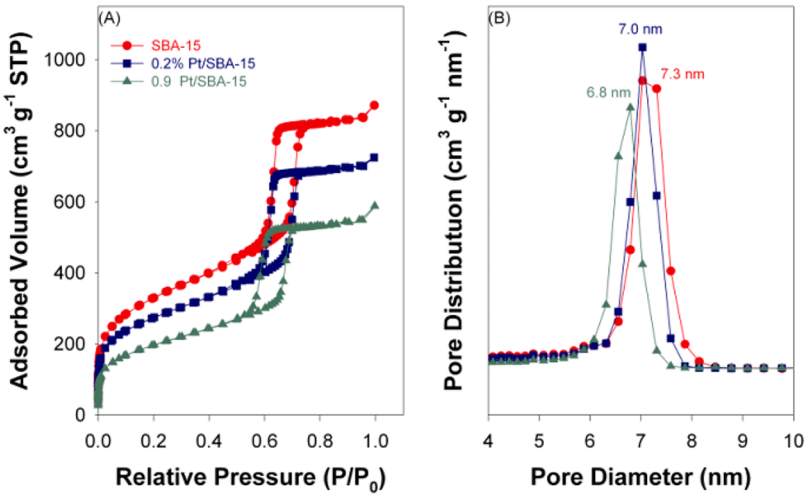

Figure 2. (A) N_2 adsorption−desorption measurements for the SBA-15 and Pt/SBA-15 samples. (B) Pore size distributions of the SBA-15 and Pt/SBA-15 samples.

Table 1. Textural Properties of SBA-15 and Pt/SBA-15[a]

sample	2θ	d_{100} (nm)	a_0 (nm)	D_{DFT} (nm)	V_t ($cm^3\ g^{-1}$)	S_{BET} ($m^2\ g^{-1}$)
SBA-15	0.96	9.2	10.7	7.3	1.3	1116
0.2 wt % Pt/SBA-15	0.97	9.1	10.5	7.0	1.1	926
0.9 wt % Pt/SBA-15	1.00	8.8	10.2	6.8	0.85	677

[a]In the table, a_0: unit cell parameter; D_{DFT}: mesopore diameter; S_{BET}: BET surface area; V_t: total pore volume.

Table 2. Characterization of Pt/SiO_2 and Pt/SBA-15 Catalysts

catalyst	CO adsorption (μmol/g cat.)	Pt surface area[a] (m^2/g)	Pt particle size[b] (nm)
0.2 wt % Pt/SBA-15	0.97	0.48	nd[c]
0.9 wt % Pt/SBA-15	2.40	1.19	5.8
0.2 wt % Pt/SiO_2	0.86	0.42	6.0
0.9 wt % Pt/SiO_2	2.15	1.06	12.8

[a]Estimate from CO chemisorption. [b]Estimate from the XRD spectra in Figure S1. [c]the XRD pattern was too weak to be observed.

benzene, and H_2 peaks were simultaneously present at ca. 385 K. The desorption of H_2 occurred at 385 K with a small peak, and substantial quantities of H_2 were generated at temperatures greater than 514 K. When the dosing amount of toluene was increased to 5 and 10 μL, a new peak associated with benzene desorption was observed at 550 K. The intensity of the high-temperature desorption peak of benzene was enhanced with increasing toluene coverage, which was accompanied by a significant decrease in the area of the H_2 peak at 385 K and in the amount of H_2 evolved at higher temperatures. The TPD profile of toluene on the pure SBA-15 support is shown in Figure S2, which shows that toluene desorbed at ca. 363 K and no detectable benzene was observed. This result implies that the SBA-15 support did not have the ability to dissociate the toluene molecule. The TPD profile of the benzene desorbed from Pt/SBA-15, which produced a single desorption peak at 385 K, is shown in Figure S3. These results suggest that the dissociation of toluene to benzene might have occurred before benzene desorbed from the Pt/SBA-15 surface at 385 K. Similar TPD experiments with toluene were performed on 0.9 wt % Pt/SiO_2, as shown in Figure S4; these experiments exhibited that only toluene desorbed at 385 K. No further reaction regarding the dissociation of toluene to benzene or H_2 was observed by the QMS.

In light of the previously described results, it is clear that the dissociation of toluene on Pt/SBA-15 at low temperatures could be reasonably reflected in the high activity of toluene oxidation. Figure 6 compares the TPD profiles of 10 μL doses of toluene (C_6H_5-CH_3) and isotopic toluene (C_6H_5-$^{13}CH_3$) on oxygen precovered Pt/SBA-15. The preadsorption of O_2 was performed by passing an air stream with a 100 mL/min flow rate through the catalyst at 298 K for 5 min. Because of the preadsorption of oxygen, intense desorption peaks of CO_2 at 356 and 406 K and peaks for toluene, benzene, and H_2 at 385 K were observed, as shown in Figure 6A. The peaks for H_2 and benzene were weak because of the coadsorption of oxygen. Interestingly, the peak associated with H_2 desorption at high temperatures and the peak associated with benzene desorption at 550 K completely vanished. These results suggest that the CH_x species generated from the decomposition of toluene are likely oxidized by the oxygen adsorbed onto the Pt/SBA-15 surface. As shown in Figure 6B, the $^{12}CO_2$ (44 amu) and $^{13}CO_2$ (45 amu) generated from the oxidation of C_6H_5-$^{13}CH_3$ were observed to desorb at 356 and 406 K, indicating that the formation of $^{12}CO_2$ and $^{13}CO_2$ might result from the oxidation of the phenyl and methyl groups in toluene, respectively. However, the TPD results of C_6H_5−CH_3 and C_6H_5-$^{13}CH_3$ on oxygen precovered Pt/SiO_2 revealed that the $^{12}CO_2$ and $^{13}CO_2$ simultaneously desorbed over a wide range of temperatures, with a maximum desorption at 470 K, as shown in Figure 7.

3.4. IR Spectra of CO Adsorbed on Pt/SBA-15 and Pt/SiO_2. Figure 8 compares the IR spectra of the CO adsorbed on the Pt/SBA-15 and Pt/SiO_2 catalysts at room temperature. The vibrational frequency of the IR bands at frequencies greater than 2000 cm^{-1} was assigned to linear CO adsorption on the Pt surfaces. Figure 8A presents the results of CO adsorbed on 0.9 and 0.2 wt % Pt/SBA-15; this figures shows that the IR peaks

dx.doi.org/10.1021/cs500733j | ACS Catal. 2014, 4, 3824−3836

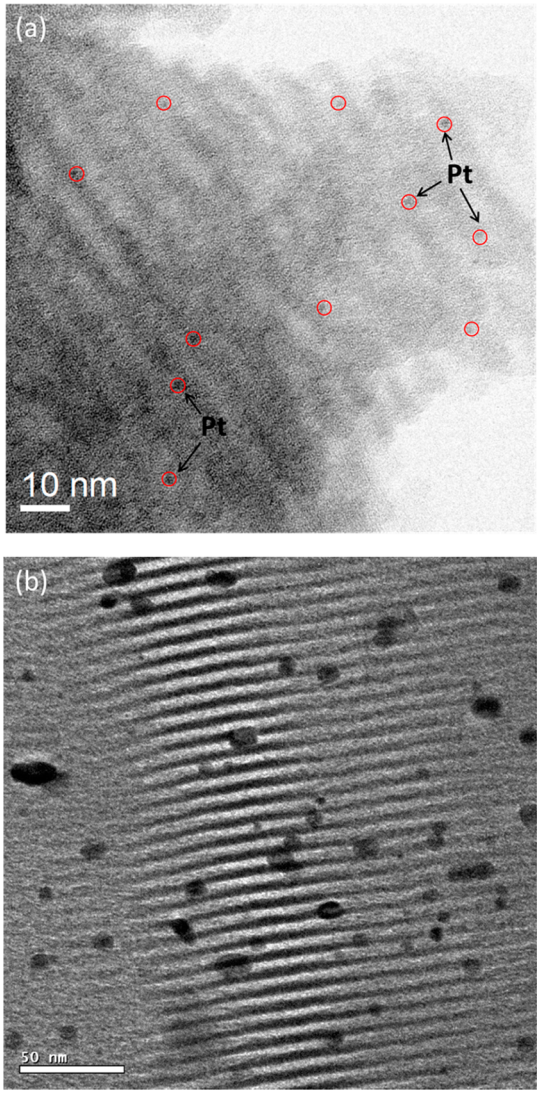

Figure 3. HRTEM images of (a) 0.2 wt Pt/SBA-15 and (b) 0.9 wt % Pt/SBA-15.

were primarily positioned at 2088 cm^{-1} (L_1 CO), 2070 cm^{-1} (L_2 CO), 2025 cm^{-1} (L_3 CO), and 2003 cm^{-1} (L_4 CO). Comparing the relative intensities for these absorption peaks on both Pt/SBA-15 catalysts, the intensities of the L_1 and L_2 CO peaks were slightly decreased, but those for the L_3 and L_4 CO peaks were significantly enhanced in relative area as the Pt loading decreased to 0.2 wt %. Figure 8B shows the IR spectra for the saturated adsorption of CO on 0.2 and 0.9 wt % Pt/SiO_2. The IR peaks of CO adsorbed on reduced Pt/SiO_2 primarily appeared at 2092 cm^{-1} (L_1 CO) and 2070 cm^{-1} (L_2 CO). The relative ratio of L_2/L_1 was enhanced as the Pt concentration decreased. However, the IR peaks of L_3 and L_4 CO could not be found on these Pt/SiO_2 catalysts.

3.5. IR Spectra of CO and Toluene Coadsorbed on Pt/SBA-15 and Pt/SiO_2. Figure 9A shows the IR spectra for CO and toluene coadsorbed on 0.9 wt % Pt/SBA-15 at room temperature. A magnified view of the spectrum associated with CO adsorption is provided (Figure 9B). The IR spectrum of toluene adsorbed on Pt/SBA-15 exhibited the characteristic bands for adsorbed toluene with ν(C−H) signals at 2824−3135 cm^{-1} and ν(C═C) peaks at 1496 and 1602 cm^{-1}. When CO adsorbed on the toluene-precovered Pt/SBA-15, the spectrum primarily revealed that the L_1 CO at 2088 cm^{-1} and L_2 CO at 2070 cm^{-1} remained on the surface. The IR peaks at 2025 cm^{-1} (L_3 CO) and 2003 cm^{-1} (L_4 CO) in Figure 9A completely disappeared, indicating that CO adsorption on the L_3 and L_4 sites was inhibited due to the preadsorption of toluene. Similar experimental results were also observed on 0.2 wt % Pt/SBA-15, as shown in Figure S5. Figure 10 compares the IR spectra of toluene adsorbed on 0.9 wt % Pt/SiO_2 and CO adsorbed on the toluene-precovered 0.9 wt % Pt/SiO_2 at room temperature. When Pt/SiO_2 was precovered with toluene, the intensity of the L_1 CO peak at 2092 cm^{-1} was significantly decreased. On Pt/SiO_2, toluene was reasonably suggested to adsorb on the L_1 site (CO at 2092 cm^{-1}).

TPD results in Figure 5 have shown that the bond breaking between phenyl and methyl groups of toluene could occur on Pt/SBA-15 catalysts. The dependence between active site on Pt/SBA-15 surface and toluene dissociation was further explored using the IR spectroscopy for coadsorption of CO

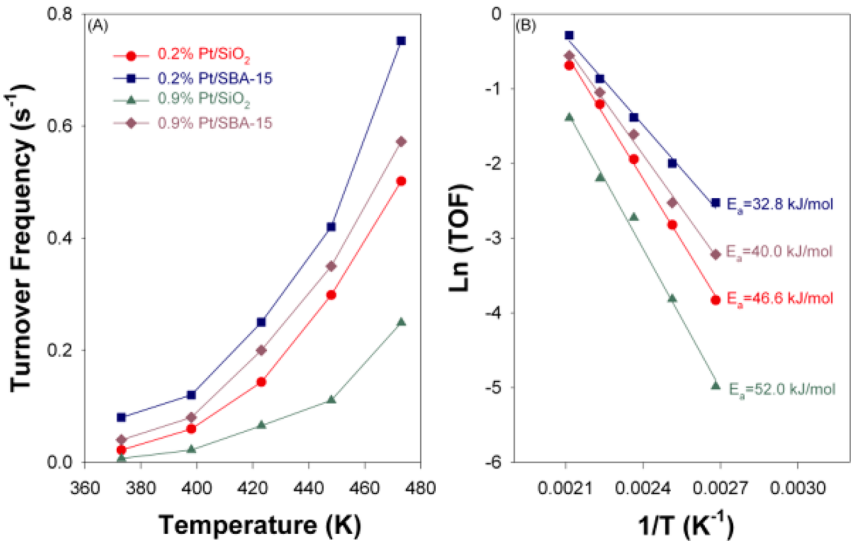

Figure 4. Comparison of the turnover frequency in toluene oxidation between the Pt/SiO_2 and Pt/SBA-15 catalysts for (A) the temperature-dependent reactions and (B) Arrhenius plots.

dx.doi.org/10.1021/cs500733j | ACS Catal. 2014, 4, 3824−3836

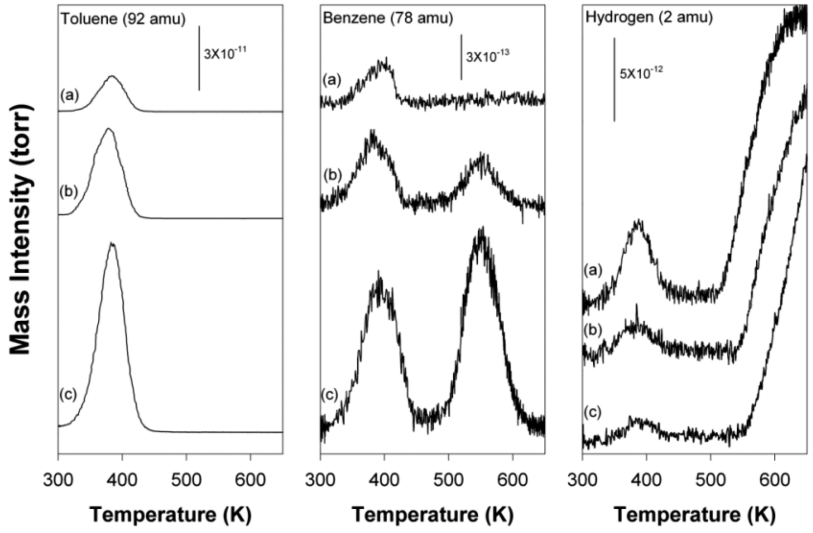

Figure 5. Temperature-programmed desorption spectra of toluene adsorbed onto 0.9 wt % Pt/SBA-15 for doses of (a) 1 μL, (b) 5 μL, and (c) 10 μL. The toluene adsorption was performed through the injection of liquid toluene at 298 K.

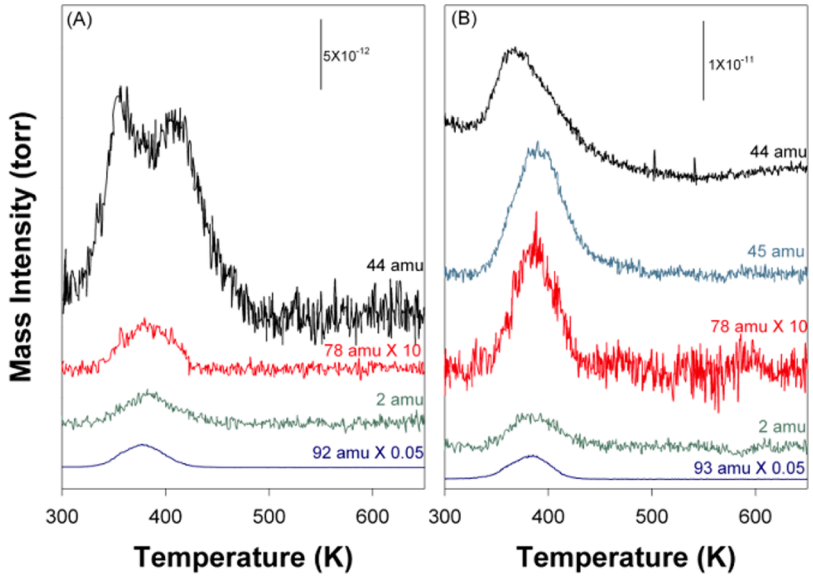

Figure 6. Temperature-programmed desorption spectra of toluene adsorbed onto oxygen-precovered 0.9 wt % Pt/SBA-15: (A) 10 μL dose of toluene (C_6H_5-CH_3); (B) 10 μL dose of isotopic toluene (C_6H_5-$^{13}CH_3$). The oxygen preadsorption was performed by passing an air stream with a 100 mL/min flow rate through the catalyst at 298 K for 5 min.

and toluene. Figure 11 depicts the result of 1 μL of toluene liquid onto toluene adsorbed on 0.9 wt % Pt/SBA-15 at 393 K in a helium stream, revealing that only ν(C−H) signals could be observed in spectrum (a). It was suggested that the decomposition reaction may generate on Pt/SBA-15, because the characteristic ν(C═C) bands of phenyl group were fully absent. The presence of ν(C−H) bands may be ascribed to the adsorbed residual hydrocarbon fragments derived from toluene decomposition. When the CO adsorbed on the surface of Pt/SBA-15 covered with the hydrocarbon fragments at 298 K, it was found that the adsorption of L_3 and L_4 CO was also completely inhibited due to the hydrocarbon fragments occupied, as shown in spectrum (b). These results demonstrated that the reaction of toluene dissociation may occur at L_3 and L_4 sites.

3.6. IR Spectra of Toluene Adsorbed on Pt/SBA-15 in an Air Stream. Figure 12A presents the in situ IR spectra of the transient toluene oxidation that was performed by injecting 1 μL of toluene liquid onto 0.9 wt % Pt/SBA-15 at 473 K in an air stream. Initially, the spectrum after injecting toluene for 1 min showed evident ν(C−H) signals and weak ν(C−O) signals for CO_2 and CO peaks. The characteristic ν(C═C) bands for the phenyl group of toluene could not be observed. The CO_2 and CO peaks were enhanced in intensity, with a strong oxidation reaction generated at 5 min. The same experiment was conducted on the 0.9 wt % Pt/SiO_2 catalyst, as shown in Figure 12B. The IR characteristic peaks of toluene, including the ν(C═C) for the phenyl group and ν(C−H), were observed in the initial reaction, but the CO peak was absent during the reaction period, even if the CO_2 product had been formed in the oxidation process. These results implied that the toluene oxidation reaction should follow different reaction pathways on both Pt/SBA-15 and Pt/SiO_2.

dx.doi.org/10.1021/cs500733j | ACS Catal. 2014, 4, 3824−3836

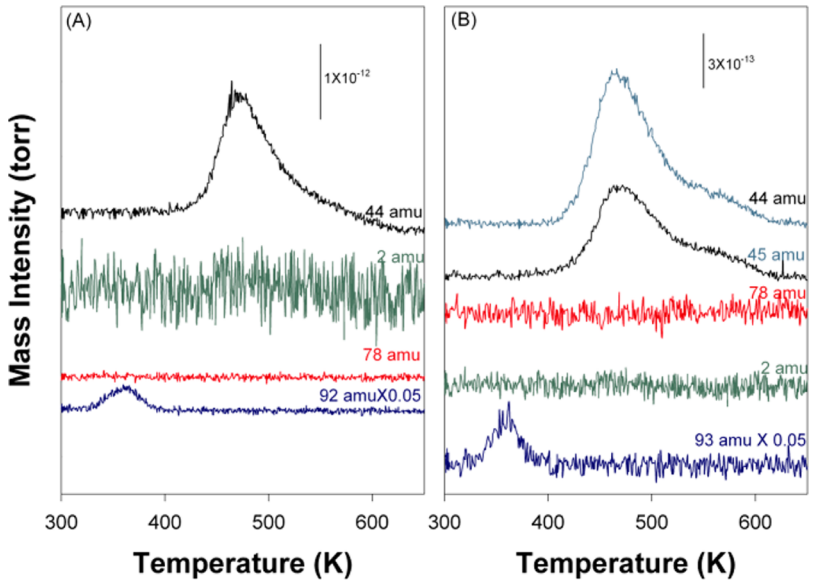

Figure 7. Temperature-programmed desorption spectra of toluene adsorbed onto oxygen-precovered 0.9 wt % Pt/SiO_2: (A) 10 μL dose of toluene (C_6H_5-CH_3); (B) 10 μL dose of isotopic toluene (C_6H_5-$^{13}CH_3$). The oxygen preadsorption was performed by passing an air stream with a 100 mL/min flow rate through the catalyst at 298 K for 5 min.

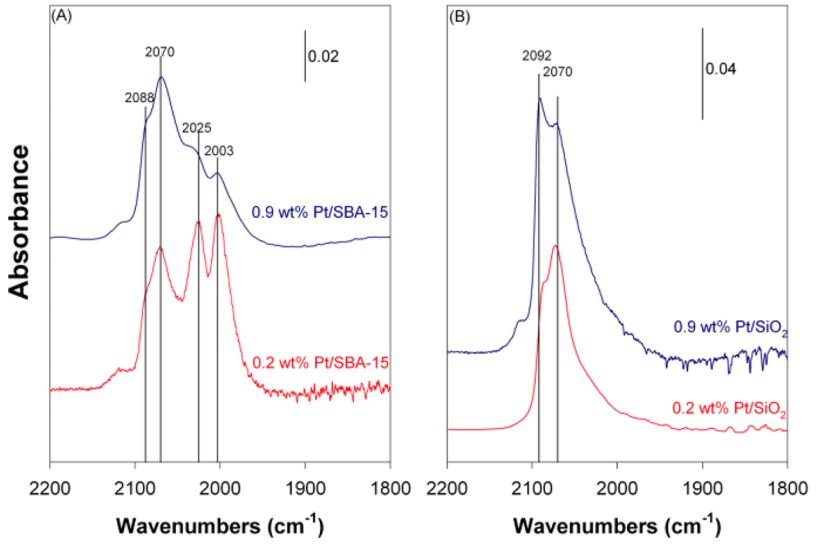

Figure 8. IR spectra of the CO adsorbed onto the reduced (A) Pt/SBA-15 and (B) Pt/SiO_2 at 298 K.

3.7. DFT Calculations. Recently, DFT calculation has been increasingly being used to predict the interactions of CO with different Pt crystal surfaces.[29−36] In this work, the L_3 CO (2025 cm^{-1}) and L_4 CO (2003 cm^{-1}) sites were proposed to the likely active sites on Pt/SBA-15 for toluene adsorption. However, DFT calculation of CO adsorbed on Pt cluster as model of highly dispersed particles has still attracted little attention in previous studies. Thus, the DFT method was used to further simulate the vibrational frequency of CO adsorbed on Pt nanoparticles for comparing the experimental results. To model nanoparticles (0.56−1.24 nm size), three isotropic types of Pt cluster structure, the icosahedron (Ih), decahedron (Dh), and truncated octahedron (Oh) were considered to generate in the DFT calculation systems, as shown in Table 3. Herein, the stretching frequencies of CO adsorbed on atop Pt sites of the cluster and terrace surface were calculated. The periodic surface slabs of four physical layers' thickness were used, with a 20 Å vacuum region between the slabs. The adsorbate and the half layers of metal were allowed to relax in all of the geometry optimization calculations without symmetry restriction.

Table 4 reveals the calculated frequency of CO on the vertex Pt sites on three periodic surfaces of (210), (100), and (111) generated from Oh and Dh clusters and one specific C_5-vertex cluster cut from the Ih and Dh clusters. It can obtain the stretching frequencies of CO adsorbed on different vertex sites with 2063 cm^{-1} for (210) plane, 2045 cm^{-1} for (100) plane, 2021 cm^{-1} for (111) plane, and 1994 cm^{-1} for C_5-vertex cluster surface. On the other hand, the distances of Pt−C and C−O bonding and the charge densities of Pt sites for CO adsorption are also compared. It is well-known that the frequency of ν(CO) closely depended on the back-donation effect between Pt and CO. The red-shift of CO frequency could be explained by more d-π* back-donation from electron-rich Pt surface to CO. Thus, it can see that the higher electron density on Pt could lead to lower stretching frequency of CO on C_5-vertex sites (Table 4).

dx.doi.org/10.1021/cs500733j | ACS Catal. 2014, 4, 3824−3836

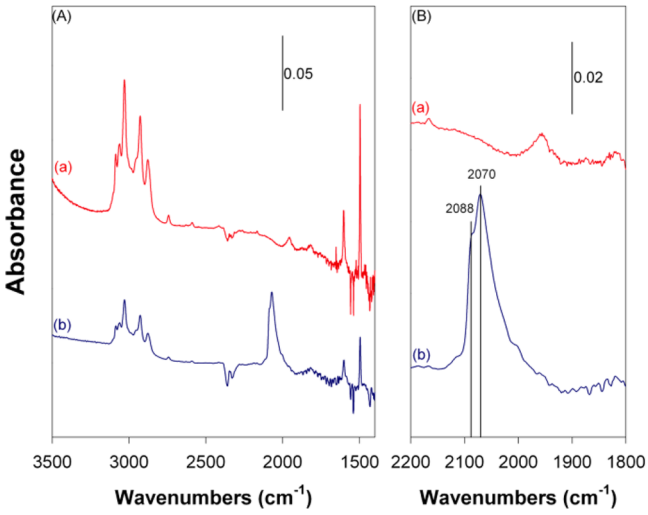

Figure 9. IR spectra for (a) a 5 μL injection of toluene onto 0.9 wt % Pt/SBA-15 and (b) CO adsorbed on the toluene-precovered Pt/SBA-15.

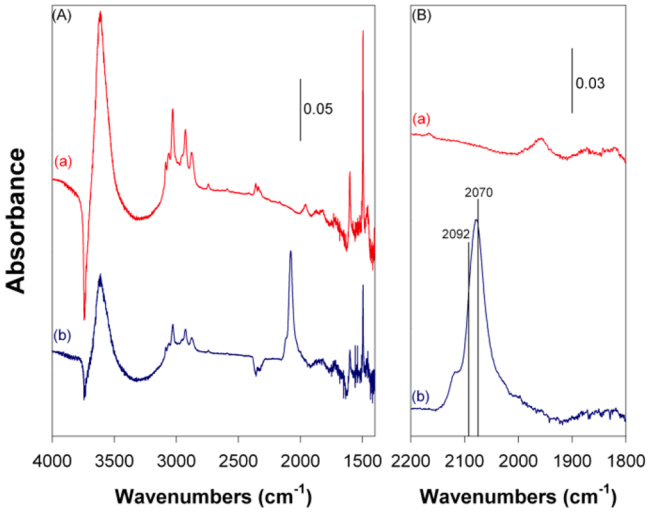

Figure 10. IR spectra for (a) 5 μL injection of toluene onto 0.9 wt % Pt/SiO_2 and (b) CO adsorbed on the toluene-precovered Pt/SiO_2.

4. DISCUSSION

4.1. Active Sites for Toluene Oxidation. The literature has indicated that the ν(CO) frequency of CO adsorbed on Pt surfaces is usually sensitive to the particle size and shifts to lower wavenumbers as the Pt coordination number decreases.[37] The assignments of the IR frequencies for CO adsorbed on Pt surfaces have been reported in the literature.[38−43] According to the literature, the band located at ca. 2090 cm^{-1} (L_1 CO) can be assigned to CO adsorbed onto the close-packed terrace sites. The frequency band at 2075 cm^{-1} (L_2 CO) in the IR spectra of CO adsorbed onto Pt surfaces corresponds to CO on defect sites, such as edges and kinks.[38−43] The band at 2025 cm^{-1} (L_3 CO) is assigned to CO adsorbed on Pt atoms of small particles.[37] Bazin et al. reported that the ν(CO) at ~2010 cm^{-1} might correspond to linear CO adsorbed on very small Pt particles (<1.5 nm) with low coordination and that the band at 2008 cm^{-1} was attributed to CO adsorbed on Pt sites with very low coordination.[37] In our experience, the literature contains no reports regarding the IR peak of linear ν(CO) positioned at 2003 cm^{-1}.

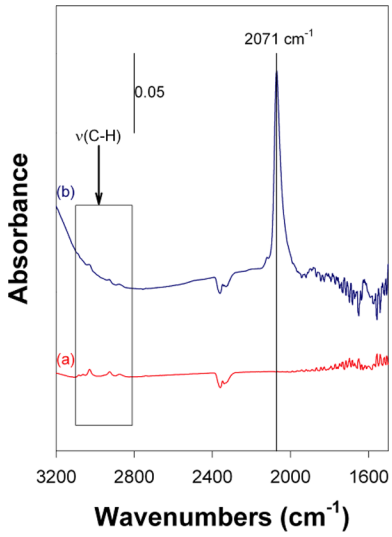

Figure 11. IR spectra for (a) a 1 μL injection of toluene onto 0.9 wt % Pt/SBA-15 at 393 K in helium stream for 10 min and (b) CO adsorbed on the toluene precovered Pt/SBA-15 at 298 K after (a).

In previous studies, DFT theoretical calculation has been used to investigate CO adsorbed on finite Pt cluster and slabs as Pt model surfaces for C−O stretching frequency.[29−36] Watwe et al. have studied the CO adsorption on neutral and charged 10-atom Pt cluster (Pt_{10}).[34] It can give the results that the stretching frequency of CO had a calculated value of 2050 cm^{-1} for neutral Pt cluster, but the negative charge on Pt_{10} cluster can cause a significant red-shift to 2020 cm^{-1} in stretching frequency.[34] Illas and his co-workers revealed the DFT calculations of CO bound to Pt_4, Pt_{10}, and Pt_{13} clusters to have the ν(CO) with 2073, 2139, and 2131 cm^{-1}, respectively.[36] The DFT calculations for CO adsorption on Pt single crystal surfaces in the literature have reported a vibrational frequency of ν(CO) with 2033−2158 cm^{-1} on Pt(111) and with 2043−2106 cm^{-1} on Pt(211).[29,30] Nevertheless, the calculations found in the literature are still insufficient for interpreting the vibrational frequency of ν(CO) near 2000 cm^{-1} in this study.

Notably, the DFT calculations in Table 4 have provided several meaningful information regarding stretching frequencies of CO adsorbed on various defect sites. The CO on the defect sites of (210), (100), and (111) from Oh and Dh clusters apparently revealed higher ν(CO) energies, but CO adsorbed on the top site of the C_5-vertex cluster derived from Ih and Dh structures represented a significant red-shift of ν(CO) at 1994 cm^{-1} due to the electron-rich surface. It is noteworthy that the Ih and Dh clusters contain 12 and 2 C_5-vertices, respectively. The phase diagram of particle size versus cluster structure has been reported in literature, suggesting that the Ih cluster is thermodynamically favored with the reduced size; the increased cluster size can tend toward the growth of Dh structure.[44] The low frequency band at 2003 cm^{-1} was in agreement with the calculated value of 1994 cm^{-1}, which could be assigned to the CO adsorbed on the electron-rich Pt cluster. The results suggest a likelihood of the low ν(CO) at 2003 cm^{-1} (L_4 CO) with respect to CO adsorbed on the defects of subnanosized Pt particles and/or a single Pt atom.

A variety of TPD experiments on toluene with and without O_2 coadsorption on Pt/SBA-15 and Pt/SiO_2 catalysts have shown that the toluene dissociation reaction might strongly

dx.doi.org/10.1021/cs500733j | ACS Catal. 2014, 4, 3824−3836

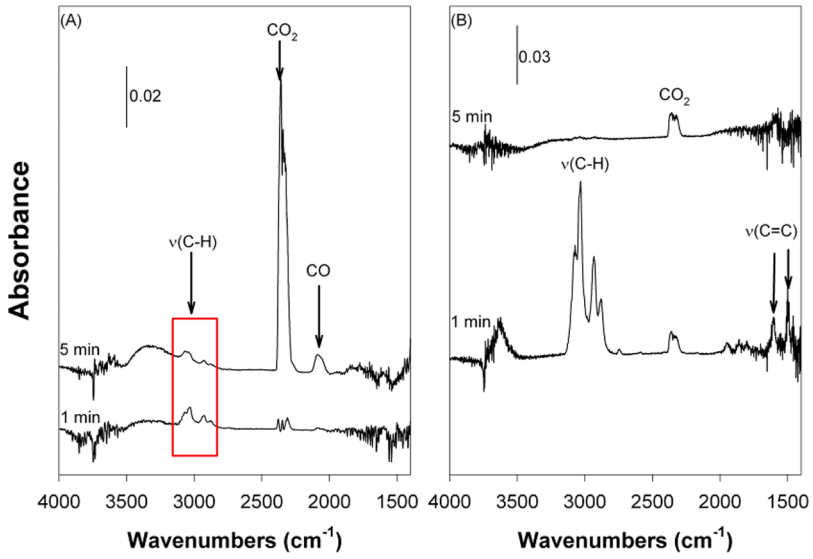

Figure 12. Time-dependent IR spectra of the pulse reaction of toluene oxidation on (A) 0.9 wt % Pt/SBA-15 and (B) 0.9 wt % Pt/SiO_2 for 1 and 5 min. The reaction was performed by injecting 1 μL of toluene onto Pt/SBA-15 in an air stream at 473 K.

Table 3. Three Types of Pt Cluster Structure, the Truncated Octahedron (Oh), Decahedron (Dh), and Icosahedron (Ih)[a]

runcated Octahedron (Oh)	Decahedron (Dh)	Icosahedron (Ih)
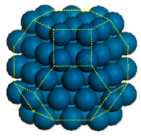	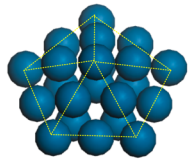	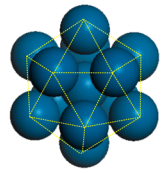
79 atoms / 1.24 nm	22 atoms / 0.3-0.9 nm	13 atoms / 0.57 nm

[a]The yellow lines indicate the cluster edges for easy identification.

depend on the activity of the Pt catalysts. IR spectroscopy was used to probe the active sites on Pt/SBA-15 and Pt/SiO_2 for the adsorption of toluene. In this work, four principal peaks corresponding to CO adsorbed on reduced Pt/SBA-15, positioned at 2088 (L_1 CO), 2070 (L_2 CO), 2025 (L_3 CO), and 2003 (L_4 CO) cm^{-1} could be observed, and the relative intensities of the L_3 and L_4 CO peaks increased as the Pt loading decreased. On the basis of the results of the IR spectra of CO adsorption, the sites for toluene adsorption could be clearly identified from the IR spectra of CO and toluene coadsorbed on Pt/SBA-15 and Pt/SiO_2. The IR spectra presented in Figure 10 indicate that toluene precovered on Pt/SiO_2 could inhibit the adsorption of CO at the L_1 site (2092 cm^{-1}). Thus, this result indicated that the toluene might prefer to adsorb on the close-packed terrace sites. On Pt/SBA-15, the toluene molecules should tend to bind on the L_3 and L_4 sites that can induce the dissociation of toluene on the Pt/SBA-15 surface. The dissociation process was assumed to be the essential step for enhancing the activity of the Pt/SBA-15 catalysts. Thus, the better turnover rate for toluene oxidation of the 0.2 and 0.9 wt % Pt/SBA-15 catalysts might depend on the higher population of L_3 and L_4 sites on the surface. Conversely, the L_1 and L_2 sites were proposed to be the major active sites for the adsorption of toluene on the Pt/SiO_2 catalysts, but they

Table 4. DFT Calculations of CO Adsorption on Pt Clusters

Surface	(210)	(100)	(111)	Cluster Pt_{22} (C_5-vertex)
Cluster	Oh	Oh, Dh	Oh, Dh, Ih*	Dh, Ih
Top View	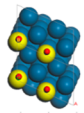	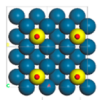	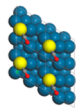	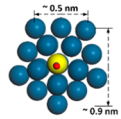
Side View	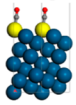		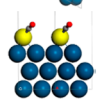	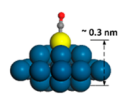
ν(C-O)/cm^{-1}	2063	2045	2021	1994
d_{Pt-C}/Å	2.014	2.001	1.998	1.965
d_{C-O}/Å	1.153	1.153	1.152	1.156
Mulliken charge of Pt	0.050	0.110	0.130	0.184

dx.doi.org/10.1021/cs500733j | ACS Catal. 2014, 4, 3824−3836

exhibited low activity for toluene oxidation due to nonreactive toward toluene decomposition.

Recently, catalysts composed of single Pt atoms on Fe_2O_3 and Al_2O_3 for the oxidation of CO have been reported in the literature; the supported single Pt atoms exhibited extremely high activity for CO oxidation and PROX reactions.[42,43,45] In contrast, a single Pt atom was also developed for synthesizing a Pt/graphene catalyst using the atomic layer deposition technique. The application of the single Pt atom catalyst in an electrocatalytic reaction showed excellent performance for the methanol oxidation reaction and superior CO tolerance.[43] The reaction of benzene steam reforming was investigated on Rh catalysts, indicating that the small Rh clusters could cause the benzene decomposition which occurred on surface and thus can enhance the catalytic reactivity.[46] These studies have suggested that very small and/or single-atom metal catalysts can positively enhance the catalytic efficiency. Notably, SBA-15 material apparently possessed the key property that might lead to the formation of tiny and subnanosized Pt particles (L_3 and L_4 sites).

In reality, the structure of the SBA-15 support should consist of a 2D hexagonal array of cylindrical mesopores, a secondary pore network, and micropores.[47] The effect of micropores in SBA-15 for synthesizing metal particles has generally attracted little attention in the literature, because the related information on the sizes and shapes of the micropores was difficult to obtain. Recently, the micropores in SBA-15 were directly measured to have a diameter between 0.57 and 0.62 nm.[47] The intrawall micropores can significantly contribute to ~30% of the total pore volume of mesoporous SBA-15.[48] The literature has indicated that Fe, Al, and Cu metals can be uniformly distributed in the intrawall micropores of SBA-15.[49] In this study, the subnanosized particles or single atoms may be confined in the micropore of SBA-15. The Ih cluster containing rich C_5-vertices may dominate the major structure of Pt particles in the micropore.

4.2. Reaction Pathway for Toluene Oxidation. A TPD study of toluene on single-crystal Pt(111) reported that the desorbed molecules included toluene and hydrogen and that aliphatic C−H bond breaking occurred more readily than aromatic C−H bond breaking on the Pt surface.[50] The decomposition of toluene mainly resulted from breakage of the C−H bond of the methyl group, indicating that hydrogen evolution might occur on the Pt surface in the thermal desorption process. In this work, the dissociation of toluene on Pt/SBA-15 followed a different mechanism compared with the previous study. A mechanism for the decomposition and catalytic oxidation of toluene was developed and is shown in Figure 13. Breaking of the C−C bonds between the phenyl and methyl groups might occur on Pt/SBA-15, leading to benzene and H_2 molecules being desorbed in the toluene-TPD spectra (Figure 5). Benzene and H_2 molecules appeared to be competitively generated at 385 K during the TPD process. It was reasonably deduced from the mechanism that the phenyl ($-C_6H_5$) and methyl ($-CH_3$) intermediates form at a temperature of less than 385 K, and then hydrogen atoms derived from the decomposition of $-CH_3$ species might either directly generate H_2 or combine with the phenyl intermediate to form benzene molecules that desorb at 385 K. Furthermore, the desorption of benzene at 550 K might not form a complete benzene molecule through the decomposition of toluene because no benzene could be detected at the high temperature in the benzene TPD result on Pt/SBA-15 (Figure S3). This

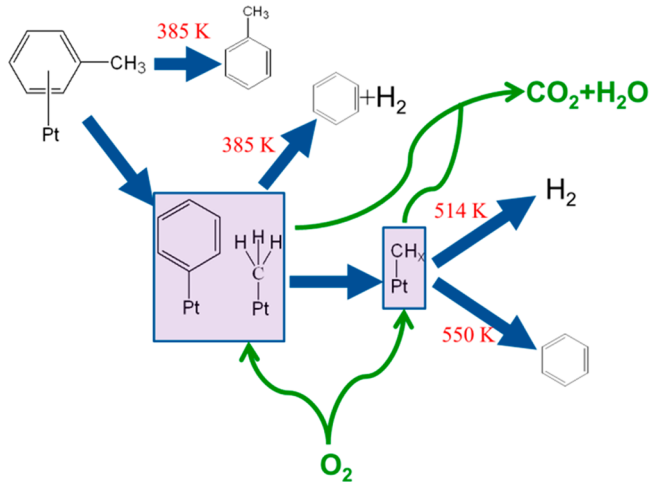

Figure 13. Proposed mechanism for the decomposition and catalytic oxidation of toluene on Pt/SBA-15.

may instead depend on the aromatization of CH_x species. The large amount of hydrogen desorption at high temperatures was attributed to the dehydrogenation of CH_x species.

The reaction mechanism and intermediates for the oxidation of toluene on the Pt(111) surface have been reported in the literature, which reported that the formation of dehydrogenated toluene can be considered the essential step in the catalytic oxidation process.[51] The dehydrogenated intermediates of toluene may strongly bind on the Pt surface and prevent the adsorption of oxygen at 300−370 K; thus, the stable intermediates inhibit oxidation at temperatures below 370 K. The highly catalytic oxidation of toluene on Pt/SBA-15 could undoubtedly be ascribed to intense decomposition on the surface through breaking of the C−C bonds between the phenyl and methyl groups. The TPD results of the coadsorption of toluene and oxygen on Pt/SBA-15 (Figure 6) revealed that the oxygen adsorbed on the Pt surface could result in the disappearance of benzene and the desorption of H_2 at high temperatures due to the oxidation of CH_x species. The IR spectra of the pulse reaction of toluene oxidation on Pt/SBA-15 at 473 K (Figure 12A) could provide several clues for the toluene oxidation mechanism. It can be observed that only ν(C−H) bands were present on Pt/SBA-15 during the initial 1 min adsorption of toluene. The generation of ν(C−H) bands might be associated with residual fragments of CH_x species and phenyl intermediates that resulted from the decomposition of toluene because the ν(C═C) band corresponding to the benzene ring did not appear in the spectrum. When strong oxidation occurred, adsorbed CO_2 and CO were clearly formed, which was accompanied by the disappearance of the ν(C−H) bands. Notably, the CO present during the oxidation process might be considered the major intermediate in the pathway toward CO_2 formation.

4.3. Compensation Phenomena. The Weisz−Prater criterion for the 0.9 wt % Pt/SBA-15 and 0.9 wt % Pt/SiO_2 catalysts were calculated to have very small numbers (Table S1), indicating that the turnover rates were not affected by diffusion limitations.[52−54] In principle, values of Weisz−Prater criterion less than 0.3 can suggest negligible mass transfer limitations.[55] Using the apparent Arrhenius plots in Figure 4, the dependence of ln A_{app} versus E_{app} for all Pt/SBA-15 and Pt/SiO_2 catalysts could be obtained in Figure 14A. There was an excellent linear relation ln A_{app} = mE_{app} + C (correlation

dx.doi.org/10.1021/cs500733j | ACS Catal. 2014, 4, 3824−3836

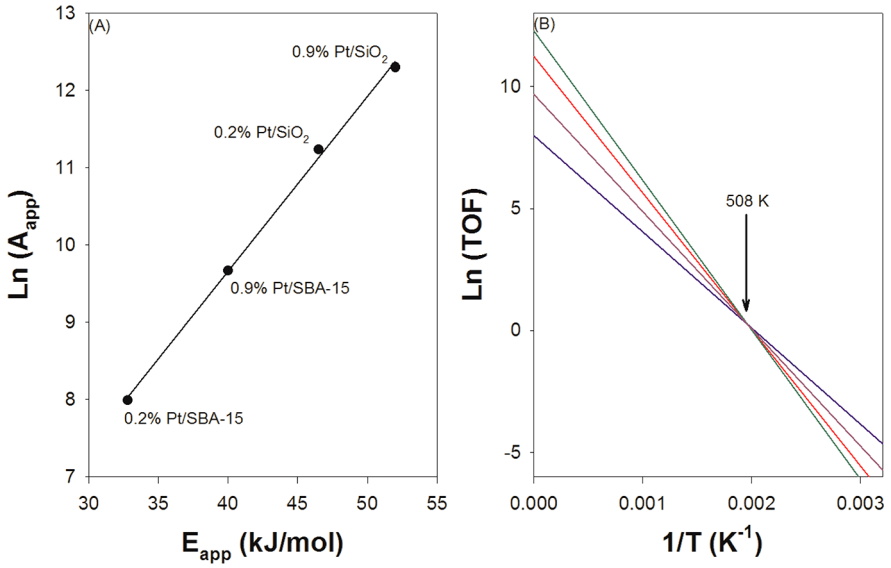

Figure 14. (A) Compensation plots for toluene oxidation over Pt/SBA-15 and Pt/SiO_2 catalysts. (B) A series of extrapolated Arrhenius plots for toluene oxidation intersecting at 508 K: the isokinetic temperature.

coefficient R^2 = 0.998), which implied that the compensation effect was present.[56−59] An increase in E_{app} was compensated by an increase in ln A_{app}. As indicated by previous studies, a true compensation relation reveals an isokinetic point that all the Arrhenius plots should intersect at a single temperature (508 K), as shown in Figure 14B. The isokinetic temperature at 508 K was derived from the slope m of the compensation plot by $m = (RT_i)^{-1}$.[56] At the isokinetic temperature, the activities for all Pt catalysts are the same. To date, there is no consistent agreement for interpreting the compensation effect. However, the compensation effect may imply the correlation for the intrinsic kinetic parameters or the correlation between the entropy and enthalpy of reactants adsorption, as the following relations:[58,59]

$$E_{app} = E_{int} + \Delta H_{ads}$$

$$\ln A_{app} = \ln A_{int} + \Delta S_{ads}$$

To study the activation energy of toluene desorption from the 0.9 wt % Pt/SBA-15 and 0.9 wt % Pt/SiO_2 catalysts, a series of TPD experiments was performed with various heating rates, as shown in Figure S6. The maximum temperature of desorption (T_{max}) for the toluene (92 amu) peaks were subsequently found to shift to higher temperatures with increasing heating rates. The Arrhenius desorption parameters were determined by the Polanyi−Wigner equation using the heating rates (β) and the maximum temperatures of desorption (T_{max}). The desorption is given by the following equation: $\ln(T_{max}^2/\beta) = (E_{des}/RT_{max}) + \ln(E_{des}/\nu R\theta_0)$. Kinetic parameters could be determined by plotting $\ln(T_{max}^2/\beta)$ as a function of $1/T_{max}$ for a series of β-values. The activation energy of toluene desorption (E_{des}) can be determined from the slopes[60,61]

However, the E_{des} values were determined to be 32.0 kJ/mol for Pt/SBA-15 and 32.9 kJ/mol for Pt/SiO_2. Pt particles on both supports apparently provided almost identical binding energy for adsorbed toluene molecules. These results suggested that the entropy and enthalpy of toluene adsorption on Pt/SBA-15 and Pt/SiO_2 may be similar, and the intrinsic kinetic parameters, such as pre-exponential factor and activation energy, were linearly correlated. Thus, it is very likely that the different reaction mechanisms of toluene oxidation on Pt/SBA-15 and Pt/SiO_2 catalysts may be the origin of the observed isokinetic relationship. The compensation effect in the rate should be intimately associated with linear relationship between entropies and enthalpies of activation in transition state. The transition state theory postulated quasi-equilibrium between reactants and a transition state can be given a rate constant by

$$k = [*]\left(\frac{k_B T}{h}\right)\exp\left(\frac{\Delta S^{\neq}}{R}\right)\exp\left(-\frac{\Delta H^{\neq}}{RT}\right)$$

where [*] represents the concentration of active sites, and $\Delta S^{\neq}$ and $\Delta H^{\neq}$ are the entropy and enthalpy of activation for the reaction to reach the transition state, respectively.[56] The pre-exponential factor A equates to the first three terms on the right-hand side: [*] $(k_B T/h)$ exp $(\Delta S^{\neq}/R)$. Therefore, it can suggest that the higher activation energy ($\Delta H^{\neq}$) on Pt catalysts may be compensated by the increase in [*]exp($\Delta S^{\neq}/R$) term. Bond at al. have proposed that the entropy−enthalpy relation leading to kinetic compensation in transition state may closely associate with the change from the set of vibrational energy level for the reactants converted to the products.[56] The energy level will be more closely spaced with increasing energy and thus enhances the probability of matching similar energy level of product sets. Therefore, the higher activation energy will increase the transition probability from reactants to products.

5. CONCLUSION

In this work, we have shown that the Pt particles loaded on SBA-15 exhibited higher catalytic activity for the oxidation of toluene than the Pt/SiO_2 catalysts. The SBA-15-supported Pt nanoparticles have the ability to strongly dissociate toluene to benzene, hydrocarbon fragments (CH_x), and H_2 at low temperatures, but the Pt/SiO_2 catalysts and SBA-15 support are nonreactive toward the decomposition of toluene. A likely mechanism is proposed in which the adsorbed toluene molecules could dissociate to phenyl ($-C_6H_5$) and methyl ($-CH_3$) intermediates, and then the hydrogen atoms derived from the decomposition of $-CH_3$ species might either directly generate H_2 or combine with the phenyl intermediates to form

dx.doi.org/10.1021/cs500733j | ACS Catal. 2014, 4, 3824−3836

benzene molecules at 385 K. The strong dissociation of toluene can effectively enhance the catalytic activity of Pt/SBA-15 for toluene oxidation. Combined DFT calculations and DRIFT spectroscopy are carried out to investigate the stretching frequency of CO adsorbed on the defect sites of various Pt clusters, suggesting that the subnanosized Pt particles (icosahedron cluster) and/or Pt single atom may be formed in the structure of SBA-15. The active sites for the adsorption of toluene on Pt/SBA-15 and Pt/SiO_2 have been identified using IR spectroscopy, showing that toluene can adsorb on the close-packed terrace sites of Pt/SiO_2 and on the sites for subnanoscale Pt particles and/or single Pt atoms of Pt/SBA-15. The Pt sites associated with low coordination and subnanoscale Pt particles and/or single Pt atoms of Pt/SBA-15 may facilitate toluene adsorption and induce strong dissociation.

■ ASSOCIATED CONTENT

Supporting Information

Calculations of Weisz−Prater criterion for the 0.9% Pt/SBA-15 and 0.9% Pt/SiO_2 catalysts; XRD spectra of Pt/SBA-15 and Pt/SiO_2; TPD spectra of toluene on pure SBA-15, benzene on 0.9 wt % Pt/SBA-15 and toluene adsorbed onto 0.9 wt % Pt/SiO_2; IR spectra for CO and toluene coadsorbed on 0.2 wt % Pt/SBA-15; toluene-TPD profiles on 0.9 wt % Pt/SBA-15 and 0.9 wt % Pt/SiO_2 catalysts with various heating rates. This material is available free of charge via the Internet at http://pubs.acs.org.

■ AUTHOR INFORMATION

Corresponding Author

*E-mail: cschen@mail.cgu.edu.tw. Fax: +886-32118700. Tel.: +886-32118800 ext. 5685.

Notes

The authors declare no competing financial interest.

■ ACKNOWLEDGMENTS

The financial support from the National Science Council of the Republic of China (NSC 100-2113-M-182-001-MY3) and Chang-Gung Memorial Hospital (CMRPD5C0021) are gratefully acknowledged.

■ REFERENCES

(1) Papaefthimiou, P.; Ioannides, T.; Verykios, X. E. *Appl. Therm. Eng.* **1998**, *18*, 1005.
(2) Delimaris, D.; Ioannides, T. *Appl. Catal., B* **2009**, *89*, 295.
(3) Hosseini, M.; Barakat, T.; Cousin, R.; Aboukaïs, A.; Su, B. L.; Weireld, G. De *Appl. Catal., B* **2012**, *111−112*, 218.
(4) Zhu, J.; Wang, T.; Xu, X.; Xiao, P.; Li, J. *Appl. Catal., B* **2013**, *130*, 197.
(5) Rodrigues, A. C. C. *Catal. Commun.* **2007**, *8*, 1227.
(6) Marsh, A. L.; Burnett, D. J.; Fischer, D. A.; Gland, J. L. *J. Phys. Chem. B* **2004**, *108*, 605.
(7) Grbic, B.; Radic, N.; Terlecki-Baricevic, A. *Appl. Catal., B* **2004**, *50*, 161.
(8) Barresi, A. A.; Cittadini, M.; Zucca, A. *Appl. Catal., B* **2003**, *43*, 27.
(9) Paulis, M.; Peyrard, H.; Montes, M. *J. Catal.* **2001**, *199*, 30.
(10) Dole, H. A. E.; Isaifan, R. J.; Sapountzi, F. M.; Lizarraga, L.; Aubert, D.; Princivalle, A.; Vernoux, P.; Baranova, E. A. *Catal. Lett.* **2013**, *143*, 996.
(11) Saqer, S. M.; Kondarides, D. I.; Verykios, X. E. *Top Catal.* **2009**, *52*, 517.
(12) Kim, K. J.; Ahn, H. G. *Appl. Catal., B* **2009**, *91*, 308.
(13) Yan, F. W.; Zhang, S. F.; Guo, C. Y.; Li, F. B.; Yan, F.; Yuan, G. Q. *Catal. Commun.* **2009**, *10*, 1689.
(14) Barresi, A. A.; Cittadini, M.; Zucca, A. *Appl. Catal., B* **2003**, *43*, 27.
(15) Radic, N.; Grbic, B.; Terlecki-Baricevic, A. *Appl. Catal., B* **2004**, *50*, 153.
(16) Zhu, J.; Xie, X.; Carabineiro, S. A. C.; Tavares, P. B.; Figueiredo, J. L.; Schomäcker, R.; Thomas, A. *Energy Environ. Sci.* **2011**, *4*, 2020.
(17) Tu, C. H.; Wang, A. Q.; Zheng, M. Y.; Wang, X. D.; Zhang, T. *Appl. Catal., A* **2006**, *297*, 40.
(18) Yoshida, K.; Arellano, C. G.; Luque, R.; Gai, P. L. *Appl. Catal., A* **2010**, *379*, 38.
(19) Chanquía, C. M.; Sapag, K.; Rodríguez-Castellón, E.; Herrero, E. R.; Eimer, G. A. *J. Phys. Chem. C* **2010**, *114*, 1481.
(20) Kumar, M. S.; Chen, D.; Walmsley, J. C.; Holmen, A. *Catal. Commun.* **2008**, *9*, 747.
(21) Wang, Z. J.; Xie, Y. B.; Lir, C. J. *J. Phys. Chem. C* **2008**, *112*, 19818.
(22) Song, H.; Rioux, R. M.; Hoefelmeyer, J. D.; Komor, R.; Niesz, K.; Grass, M.; Yang, P.; Somorjai, G. A. *J. Am. Chem. Soc.* **2006**, *128*, 3027.
(23) Friedrich, H.; Sietsma, J. R. A.; de Jongh, P. E.; Verkleij, A. J.; de Jong, K. P. *J. Am. Chem. Soc.* **2007**, *129*, 10249.
(24) Zhu, J.; Wang, T.; Xu, X.; Xiao, P.; Li, J. *Appl. Catal., B* **2013**, *130*, 197.
(25) Bendahou, K.; Cherif, L.; Siffert, S.; Tidahy, H. L.; Benaïssa, H.; Aboukaïs, A. *Appl. Catal., A* **2008**, *351*, 82.
(26) Anderson, J. R.; Pratt, K. C. *Introduction to Characterization and Testing of Catalysts*; Academic Press Inc.: Sydney, 1985; p 64.
(27) Delley, B. *J. Chem. Phys.* **2000**, *113*, 7756.
(28) Perdew, J. P.; Wang, Y. *Phys. Rev. B* **1992**, *45*, 13244.
(29) Lozovoi, A. Y.; Alavi, A. *J. Electroanal. Chem.* **2007**, *607*, 140.
(30) Orita, H.; Inada, Y. *J. Phys. Chem. B* **2005**, *109*, 22469.
(31) Moses-DeBusk, M.; Yoon, M.; Allard, L. F.; Mullins, D. R.; Wu, Z.; Yang, X.; Veith, G.; Stocks, G. M.; Narula, C. K. *J. Am. Chem. Soc.* **2013**, *135*, 12634.
(32) Manceron, L.; Tremblay, B.; Alikhani, M. E. *J. Phys. Chem. A* **2000**, *104*, 3750.
(33) Feng, X.; Yao, M.; Hu, X.; Hu, G.; Jia, A.; Xie, G.; Lu, J.; Luo, M. *Int. J. Hydrogen Energy* **2013**, *38*, 13673.
(34) Watwe, R. M.; Spiewak, B. E.; Cortright, R. D.; Dumesic, J. A. *Catal. Lett.* **1998**, *51*, 139.
(35) Feibelman, P. J.; Hammer, B.; Nørskov, J. K.; Wagner, F.; Scheffler, M.; Stumpf, R.; Watwe, R.; Dumesic, J. *J. Phys. Chem. B* **2001**, *105*, 4018.
(36) García-Hernández, M.; Curulla, D.; Clotet, A.; Illas, F. *J. Chem. Phys.* **2000**, *113*, 364.
(37) Bazin, P.; Saur, O.; Lavalley, J. C.; Daturi, M. *Phys. Chem. Chem. Phys.* **2005**, *7*, 187.
(38) Ebbesen, S. D.; Mojet, B. L.; Lefferts, L. *J. Catal.* **2007**, *246*, 66.
(39) Lundwall, M. J.; McClure, S. M.; Goodman, D. W. *J. Phys. Chem. C* **2010**, *114*, 7904.
(40) Song, H.; Rioux, R. M.; Hoefelmeyer, J. D.; Komor, R.; Niesz, K.; Grass, M.; Yang, P.; Somorjai, G. A. *J. Am. Chem. Soc.* **2006**, *128*, 3027.
(41) Daniel, C.; Clarté, M.-O.; Teh, S.-P.; Thinon, O.; Provendier, H.; Van Veen, A. C.; Beccard, B. J.; Schuurman, Y.; Mirodatos, C. *J. Catal.* **2010**, *272*, 55.
(42) Qiao, B.; Wang, A.; Yang, X. *Nat. Chem.* **2011**, *3*, 634.
(43) Moses-DeBusk, M.; Yoon, M.; Allard, L. F.; Mullins, D. R.; Wu, Z.; Yang, X.; Veith, G.; Stocks, G. M.; Narula, C. K. *J. Am. Chem. Soc.* **2013**, *135*, 12634.
(44) Doye, J. P. K.; Calvo, F. *Phys. Rev. Lett.* **2001**, *86*, 3570.
(45) Sun, S.; Zhang, G.; Gauquelin, N.; Chen, N.; Zhou, J.; Yang, S.; Chen, W.; Meng, X.; Geng, D.; Banis, M. N.; Li, R.; Ye, S.; Knights, S.; Botton, G. A.; Sham, T. K.; Sun, X. *Sci. Rep.* **2013**, *3*, 1775 DOI: 10.1038/srep01775.
(46) Mei, D.; Lebarbier, V. M.; Rousseau, R.; Glezakou, V. A.; Albrecht, K. O.; Kovarik, L.; Flake, M.; Dagle, R. A. *ACS Catal.* **2013**, *3*, 1133.

(47) Pollock, R. A.; Walsh, B. R.; Fry, J.; Ghampson, I. T.; Melnichenko, Y. B.; Kaiser, H.; Pynn, R.; DeSisto, W. J.; Wheeler, M. C.; Frederick, B. G. *Chem. Mater.* **2011**, *23*, 3828.
(48) Galarneau, A.; Cambon, H.; Renzo, F. D.; Ryoo, R.; Choi, M.; Fajula, F. *New J. Chem.* **2003**, *27*, 73.
(49) Liu, C. H.; Lai, N. C.; Liou, S. C.; Chu, M. W.; Chen, C. H.; Yang, C. M. *Microporous Mesoporous Mater.* **2013**, *179*, 40.
(50) Tsai, M. C.; Muetterties, E. L. *J. Am. Chem. Soc.* **1982**, *104*, 2534.
(51) Marsh, A. L.; Burnett, D. J.; Fischer, D. A.; Gland, J. L. *J. Phys. Chem. B* **2004**, *108*, 605.
(52) Williams, C. L.; Chang, C. C.; Do, P.; Nikbin, N.; Caratzoulas, S.; Vlachos, D. G.; Lobo, R. F.; Fan, W.; Dauenhauer, P. J. *ACS Catal.* **2012**, *2*, 935.
(53) Gosselink, R. W.; Xia, W.; Muhler, M.; de Jong, K. P.; Bitter, J. H. *ACS Catal.* **2013**, *3*, 2397.
(54) Crisci, A. J.; Tucker, M. H.; Lee, M. Y.; Jang, S. G.; Dumesic, J. A.; Scott, S. L. *ACS Catal.* **2011**, *1*, 719.
(55) Vannice, M. A. *Kinetic of Catalytic Reactions*; Springer: New York, 2005; p 65.
(56) Bond, G. C.; Frodsham, S. J.; Jubb, P.; Kozhevnikova, E. F.; Kozhevnikov, I. V. *J. Catal.* **2012**, *293*, 158.
(57) Bligaard, T.; Honkala, K.; Logadottir, A.; Nørskov, J. K.; Dahl, S.; Jacobsen, J. H. *J. Phys. Chem. B* **2003**, *107*, 9325.
(58) Oudenhuijzen, M. K.; van Bokhoven, J. A.; Koningsberger, D. C. *J. Catal.* **2003**, *219*, 134.
(59) van Bokhoven, J. A.; Williams, B. A.; Ji, W.; Koningsberger, D. C.; Kung, H. H.; Miller, J. T. *J. Catal.* **2004**, *224*, 50.
(60) Yagi, K.; Sekiba, D.; Fukutani, H. *Surf. Sci.* **1999**, *442*, 307.
(61) Wilmer, H.; Genger, T.; Hinrichsen, O. *J. Catal.* **2003**, *215*, 188.